



Microscale dispersion behaviors of dust particles during coal cutting at large-height mining face

Yao Xie¹ · Weimin Cheng^{1,2} · Haiming Yu¹ · Biao Sun¹

Received: 21 April 2018 / Accepted: 5 July 2018 / Published online: 18 July 2018
© Springer-Verlag GmbH Germany, part of Springer Nature 2018

Abstract

In order to ensure safe production and occupational health at a large-mining-height fully mechanized mining face in a coal mine, the present study firstly establishes an airflow-dust coupled model based on gas/solid two-phase flow equations and combines numerical simulation and field measurement for analyzing the dispersion pattern of dust particles with various sizes for different coal cutter locations. Results show that, due to the existence of drums, airflow deviates from the original direction and enters the footway. Driven by the airflow, dust particles enter the footway at different locations depending on coal cutter locations. The coal-cutting location (denoted as P_{ri}) and the location where dust particles enter the footway (denoted as P_{di}) are correlated as follows: $P_{di}(P_{ri}) = -0.0007P_{ri}^2 + 1.0343P_{ri} - 3.3536$. When $P_{ri} < 55$ m, dust particles produced by the rear drum during coal cutting enter the footway earlier than those produced by the front drum, leading to the first and second dust concentration peaks in respiratory zones of footway. Dust suppression effects are assessed in these regions based on the first and second dust concentration peaks. Due to the superposition of the concentration fields associated with dust particles 2.5, 7, and 20 μm in diameter, dust concentration 25 m down the leeward side of the coal cutter can reach 1440 mg/m^3 . The concentration of dust particles with a diameter of 40 μm drops steadily and approaches 0 at the return corner. The dust particles 80 μm in diameter are fully settled within 22 m down the leeward side of the coal cutter. A comparison with the field measurement indicates that the present simulation results are highly accurate.

Keywords Large mining height · Fully mechanized mining face · Cutting location · Dust sizes · Dispersion patterns

Introduction

Coal mining plays a key role in China's energy industry and always contributes greatly to promoting the nation's economic development. As the mechanization level of coal mining industry improves, more and more dust is produced, and high-concentration dust causes explosion when it comes in contact with an open flame; moreover, dissociative SiO_2 and

microorganisms in the dust also severely threaten the coal miners' physical and psychological health (Liu et al. 2017a, b).

According to the *Statistical Report of Occupational Diseases* released by National Health and Family Planning Commission each year (see Fig. 1), the total number of occupational disease cases increased from 680,071 cases in 2005 to 924,603 cases in 2016; in particular, the total number of pneumoconiosis cases increased from 607,570 cases to 831,246 cases, and the fraction of pneumoconiosis cases in all occupational diseases cases also increased from 89.34 to 89.90% (Cheng et al. 2016; Yu et al. 2017). As stated in the related safety regulations of coal mines, the time-weighted average (TWA) allowable concentrations of total dust and respirable dust cannot exceed 4 and 2.5 mg/m^3 , respectively. In underground mines, a great amount of dust is produced in fully mechanized mining faces; in particular, instantaneous dust concentrations at some operating sites can be as high as 4000–6000 mg/m^3 , which seriously violates safety regulations of coal mines (Klemens et al. 2001; Shi et al. 2008). Therefore,

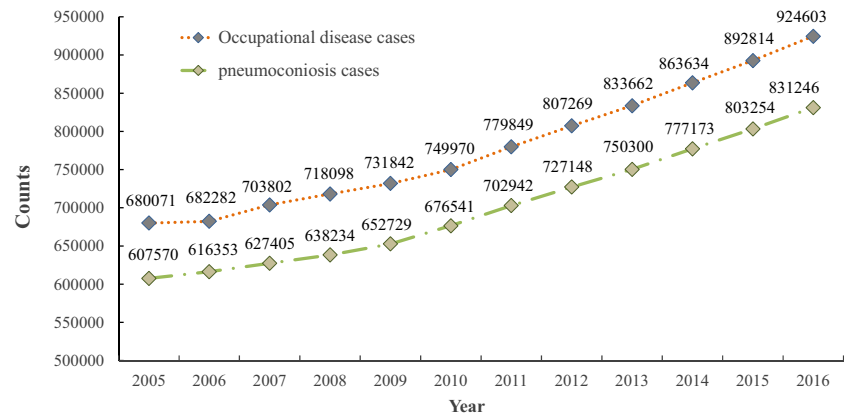
Responsible editor: Marcus Schulz

✉ Weimin Cheng
skdwmc@163.com

¹ College of Mining and Safety Engineering, Shandong University of Science and Technology, Qingdao 266590, China

² State Key Laboratory of Mining Disaster Prevention and Control Co-founded by Shandong Province and the Ministry of Science and Technology, Shandong University of Science and Technology, Qingdao 266590, China

Fig. 1 Statistics of occupational disease and pneumoconiosis cases in China from 2005 to 2016



it is of particular importance to adopt some effective dust suppression measures in fully mechanized mining faces.

At present, commonly used dust suppression measures in China's fully mechanized mining faces mainly include spraying dedusting, coal seam water injection, wet dust collection, and air curtain for dust suppression. However, due to insufficient knowledge of dust dispersion patterns in the fully mechanized mining faces, these methods fail to deliver satisfactory effects; furthermore, the respirable dust cannot be effectively suppressed and thereby continues to jeopardize the miners' health and the safe production (Fan et al. 2018; Cheng et al. 2017; Zhou et al. 2018). Fully mechanized coal mining with a large mining height, as a novel mining technology, exhibits an array of advantages, e.g., high productivity, reduced tunneling, and great yield per unit, making it widely applied in thick-coal-seam mines. Meanwhile, the coal mining in large-mining-height fully mechanized faces relies heavily on large-scale mechanization, leading to elevated dust concentration in the operating zones. Moreover, dust dispersion patterns in the large-mining-height mining faces also differ greatly from those in regular mining faces. It is thus quite necessary to gain more in-depth knowledge of dust dispersion patterns in large-mining-height fully mechanized mining faces (Liang et al. 2017; Zhang et al. 2018; Wang et al. 2016).

Scholars worldwide have performed extensive numerical simulations to investigate dust production and migration patterns in the mining faces. Hodkinson et al. investigated the variation patterns of dust concentration in a fully mechanized mining face, which revealed that the dust concentration peaks 10~20 m on the leeward side of the coal cutter (Hodkinson 1960). Courtney et al. examined the dust migration and settling behaviors in the tunnels but failed to clarify the migration patterns of dust particles with different sizes in the working face (Courtney et al. 1986). Patankar et al. employed large eddy simulation and Lagrange method to gain more in-depth knowledge of airflow and dust migration and analyzed the migration behaviors of dust particles with different Stokes numbers driven by airflow (Patankar & Joseph 2001); Jia et al. studied the migration patterns of respirable dust in the fully

mechanized mining face with two ultra-long coal cutters by means of gas/solid coupled multi-phase flow simulation, based on which the main impact zones of respirable dust were identified (Jia et al. 2016). Previous studies concerning the working faces at ordinary mining depths laid emphasis on macroscale dispersion patterns of dust at some specific coal cutting locations, yet neglected the dust dispersion patterns at different positions at microscale. Moreover, most existing studies suffered from poorly processed simulation data and deficiencies in quantitative analyses, which compromised the understanding of the dispersion behaviors associated with the microscale multi-granularity dust particles. Therefore, the present study firstly establishes an accurate airflow-dust coupled model and performs extensive studies on micro-dispersion behaviors of multi-granularity dust particles in a large-mining-height mining face, which can thus provide solid foundation for developing effective dust suppression techniques in fully mechanized mining faces with large mining heights.

Methodology

Mathematical model

Mathematical model of continuous phase

In a fully mechanized mining face, the dispersion of dust with airflow in the tunnel can be regarded as solid-gas two-phase flow, while the migration of airflow can be regarded as disordered turbulent flow (Kurnia et al. 2014; Ren et al. 2014). Therefore, the dust dispersion and the turbulent airflow field in the tunnel can be described by the Euler-Lagrange model and the realizable k -epsilon model, respectively.

The continuity equation can be written as follows:

$$\frac{\partial}{\partial x_i}(\rho u_i) = 0 \quad (1)$$

The momentum equation can be written as follows:

$$\frac{\partial}{\partial x_i}(\rho u_i u_j) = -\frac{\partial p}{\partial x_i} + \rho g_i + \frac{\partial}{\partial x_j} \left[(\mu + \mu_t) \left(\frac{\partial u_i}{\partial x_j} + \frac{\partial u_j}{\partial x_i} \right) \right] \tag{2}$$

Based on the *k*-equation of turbulence energy, the turbulent energy dissipation rate, denoted as ε , is introduced, and the related mathematical models are established below (Toraño et al. 2011).

The *k*-equation can be written as:

$$\frac{\partial}{\partial t}(\rho k) + \frac{\partial}{\partial x_i}(\rho k u_i) = \frac{\partial}{\partial x_j} \left[\left(\mu + \frac{\mu_t}{\sigma_k} \right) \frac{\partial k}{\partial x_j} \right] + P_k + P_b - \rho \varepsilon - Y_M + S_k \tag{3}$$

The ε -equation can be written as:

$$\frac{\partial}{\partial t}(\rho \varepsilon) + \frac{\partial}{\partial x_i}(\rho \varepsilon u_i) = \frac{\partial}{\partial x_j} \left[\left(\mu + \frac{\mu_t}{\sigma_\varepsilon} \right) \frac{\partial \varepsilon}{\partial x_j} \right] + \rho C_1 S \varepsilon - \rho C_2 \frac{\varepsilon^2}{k + \sqrt{v \varepsilon}} + C_{1\varepsilon} \frac{\varepsilon}{k} C_{3\varepsilon} P_b + S_\varepsilon \tag{4}$$

where u_i and u_j denote the velocities (m/s) along the *x*-axis and *y*-axis, respectively; $C_1 = \max \left[0.43, \frac{\eta}{\eta+5} \right]$, $\eta = S \frac{k}{\varepsilon}$; Y_M denotes the fluctuations in the compressible turbulent flow induced by transition and diffusion; S_k and S_ε denote the defined turbulent kinetic energy; P_k denotes the generation of turbulence kinetic energy due to the mean velocity gradients, $P_k = \mu_t S^2$, where S denotes the modulus of the mean rate-of-strain tensor and is defined as: $S = \sqrt{2 S_{ij} S_{ij}}$; P_b refers to the generation of turbulence kinetic energy due to buoyancy, $P_b = \beta g_i \frac{\mu_t}{Pr_t} \frac{\partial T}{\partial x_i}$, where Pr_t is the turbulence Prandtl number for energy and g_i is the component of the gravitational vector in the *i*th direction. For the realizable *k*-epsilon model, the default value of Pr_t is 0.85. The coefficient of thermal expansion, β , is defined as: $\beta = -\frac{1}{\rho} \left(\frac{\partial \rho}{\partial T} \right)_p$; μ denotes the laminar flow viscosity coefficient (Pa s); μ_t denotes the viscosity coefficient of the turbulent flow, $\mu_t = \rho C_\mu \frac{k^2}{\varepsilon}$, where C_μ is a function of the average change rate of the turbulent flow field, $C_\mu = \frac{1}{A_0 + A_S k U^* / \varepsilon}$, U^* denotes internal energy; $U^* = \sqrt{S_{ij} S_{ij} + \tilde{\Omega}_{ij} \tilde{\Omega}_{ij}}$, $\tilde{\Omega}_{ij} = \Omega_{ij} - 2 \varepsilon_{ijk} \omega_k$, $\Omega_{ij} = \overline{\Omega_{ij}} - \varepsilon_{ijk} \omega_k$, and $\overline{\Omega_{ij}}$ is the mean rate-of-rotation tensor viewed in a rotating

reference frame with angular velocity ω_k . The constants A_0 and A_S are given by: $A_0 = 4.04$, $A_S = \sqrt{6} \cos \psi$, $\psi = \frac{1}{3} \cos^{-1}(\sqrt{6} W)$, W denotes the power, and $W = \frac{S_{ij} S_{ik} S_{ki}}{S^3}$, $\tilde{S} = \sqrt{S_{ij} S_{ij}}$, and $S_{ij} = \frac{1}{2} \left(\frac{\partial u_j}{\partial x_i} + \frac{\partial u_i}{\partial x_j} \right)$.

In Eqs. (3) and (4), $C_{1\varepsilon} = 1.44$, $C_2 = 1.9$, $\sigma_k = 1.0$, and $\sigma_\varepsilon = 1.2$.

Airflow-dust coupled simulation model

The dust produced during coal cutting process in a fully mechanized mining face is mainly driven by the unidirectional airflow and is thus subject to gravity, buoyancy, drag force, mass force, and pressure gradient (Nie et al. 2016; Sa et al. 2012; Zhou et al. 2017). By neglecting some second-order terms, the dust particle force balance equation can be written as:

$$\frac{d \vec{u}_p}{dt} = \vec{F}_D (\vec{u} - \vec{u}_p) + \frac{\vec{g} (\rho_p - \rho)}{\rho_p} \tag{5}$$

where $d \vec{u}_p / dt$ denotes the inertial force of the dust particle with unit mass, in which \vec{u}_p denotes the particle speed vector; $\vec{F}_D (\vec{u} - \vec{u}_p)$ denotes the drag force on particles per unit mass, wherein \vec{u} is the air velocity vector, and \vec{u}_p is the particle velocity vector, F_D can be calculated as follows: $F_D = \frac{18 \mu}{\rho_p d_p^2} \frac{C_D Re}{24}$; $\vec{g} (\rho_p - \rho) / \rho_p$ denotes the sum of the gravity and buoyancy on particles per unit mass, in which ρ is the air density, and ρ_p denotes the density of dust particle.

Re denotes the particle Reynolds number, which can be calculated as:

$$Re = \frac{\rho d_p |\vec{u}_p - \vec{u}|}{\mu} \tag{6}$$

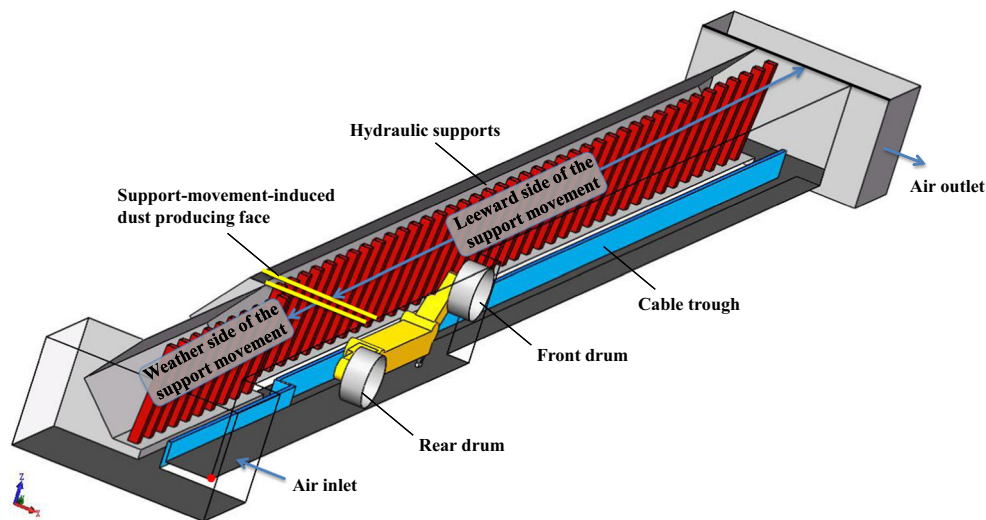
where d_p denotes the diameter of the particle in m.

The drag coefficient, denoted as C_D , can be calculated as:

$$C_D = a_1 + \frac{a_2}{Re} + \frac{a_3}{Re^2} \tag{7}$$

$$a_1, a_2, a_3 = \begin{cases} 0, 24, 0 & 0 < Re < 0.1 \\ 3.690, 22.73, 0.0903, & 0.1 < Re < 1 \\ 1.222, 29.1667, -3.8889 & 1 < Re < 10 \\ 0.6167, 46.50, -116.67 & 10 < Re < 100 \\ 0.3644, 98.33, -2778 & 100 < Re < 1000 \\ 0.357, 148.62, -47.500 & 1000 < Re < 5000 \\ 0.46, -490.546, 578.700 & 5000 < Re < 10,000 \\ 0.5191, -1662.5, 5, 416, 700 & Re > 10,000 \end{cases} \tag{8}$$

Fig. 2 Established model of the large-mining-height fully mechanized mining face for $P_{rl} = 35$ m



Establishment of physical model and the associated physical conditions

Establishment of physical model

The present study focuses on the #3 upper coal seam in no. 5301 fully mechanized mining face of Tangkou Mine with an inclination angle of 1~10°, where coal formation is simple in structure and includes no dirt bands. The mining face is 5.6-m tall, 10-m wide, and 90-m long. An array of full-scale physical models of the large-mining-height fully mechanized mining face are built with the coal cutter operated at different locations, which mainly incorporate an air inlet, a cable trough, hydraulic supports, a coal cutter, a scraper conveyer, and a return airway. P_{rl} denotes the distance between the central axis

of the coal cutter and the inlet airway and is set to 25, 35, 45, 55, and 65 m in the present study. Figure 2 shows the established physical model of the mining face for $P_{rl} = 35$ m, in which the origin denotes the point where inlet airway, mining face and scraper conveyer intersect, the positive direction of x -axis points from the footway to coal wall, the positive direction of y -axis points from inlet airway to return airway, and the positive direction of z -axis points from tunnel floor to roof. Specifically, a dual-drum coal cutter (MG750/1800-WD) 6.0 m × 1.5 m × 2.0 m in size is used, for which the rocker length is 3.0 m and the drum diameter is 2.5 m. Also, 51 hydraulic supports (ZY10000/26/55) are arranged covering the entire mining face, with the spacing between two neighboring support centers set to 1.75 m. The height of the top beam of the hydraulic support from the floor is 5.6 m; the width of the cable trough is 0.4 m.

Fig. 3 Simulation results of airflow velocity using different meshes with different densities

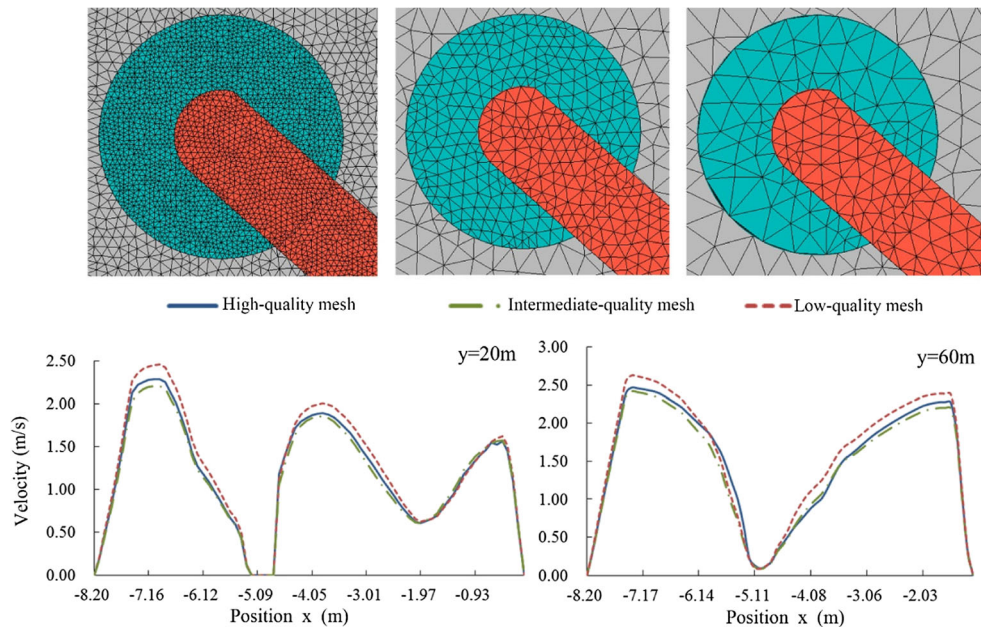
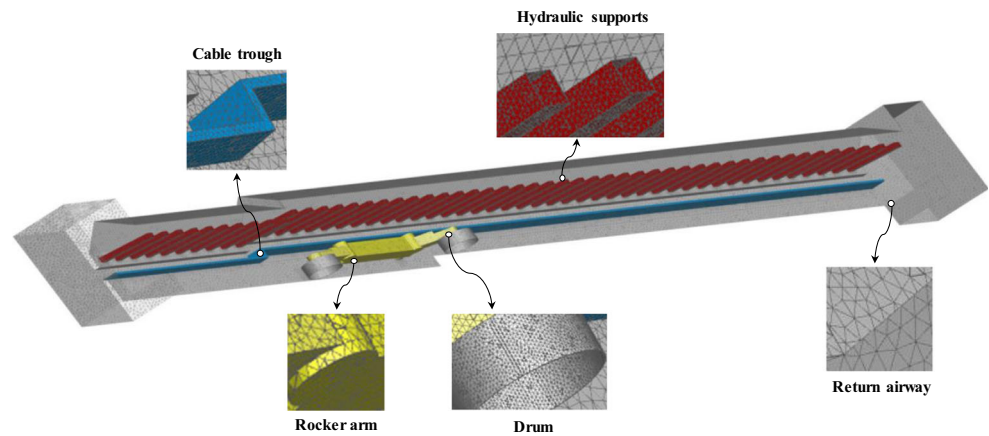


Fig. 4 The established physical model based on mesh generation



Mesh generation refers to discretizing a complex physical model into finite elements based on finite element analysis, and then solving the governing equation in each element (Cheng et al. 2012; Wang et al. 2017b; Liu et al. 2018). The quality of the generated mesh directly affects the computational accuracy and cost. Therefore, in order to ensure a decent mesh quality, the mesh size should be adjusted iteratively based on local refinement. In general, an increased cell number leads to enhanced accuracy. However, an excessively large number of grid blocks makes the computational overhead unacceptable (Wang et al. 2017a; Wang et al. 2011). Hence, it is fairly necessary to conduct mesh-independence check on the numerical results while modeling the large-mining-height fully mining faces. In the present study, three meshes with different qualities, namely, high-quality mesh, intermediate-quality mesh, and low-quality mesh, are generated using the Integrated Computer Engineering and Manufacturing code (ICEM), with the qualities of three meshes all exceeding 0.3. Since airflow velocities differ from location to location in the fully mechanized mining

face, the present study selects different locations ($z = 2.6$ m) at two tunnel cross-sections ($y = 20$ m and $y = 60$ m) for comparison, and accordingly, the effect of mesh size on the simulation results can also be examined. Figure 3 shows the comparison of airflow velocity at different locations using different meshes. It can be observed that the high-quality mesh and intermediate-quality mesh yield almost identical results, while the low-quality mesh exhibits similar variation trend yet different absolute values. This comparison indicates that the intermediate-quality mesh is most suitable for the present study, with the topology of the resulting mesh shown in Fig. 4.

Boundary conditions

In accordance with the actual ventilation condition in the no. 5301 fully mechanized mining face of Tangkou Coal Mine, boundary conditions of the airflow field are set in the model as follows: the airway inlet is set as “velocity inlet”; the airway outlet is set as “pressure outlet” with a pressure of 1 atm such

Table 1 Parameters in airflow-dust simulations

Variable	Type	Property	Value
Air-flowing	General	Solver type	Pressure-based
		Time	Steady
	Model	Viscous	<i>k</i> -epsilon realizable
	Air	Density	1.225 kg/m ³
		Viscosity	1.7894e-05 kg/m s
	Inlet	Velocity inlet	1.3 m/s
Dust	Solution methods	Scheme	SIMPLEC
	Materials	Fluent inert particle materials	Coal-hv
		Density	1400 kg/m ³
	Tracking parameters	Max. number of steps	500,000
		Step length factor	5
	Injection properties	Injection type	Surface
		Particle type	Inert
	Point properties	Diameter	2.5 μm, 7 μm, 20 μm, 40 μm, 80 μm
		Total flow rate	0.025 kg/s
	Physical models	Drag law	Spherical

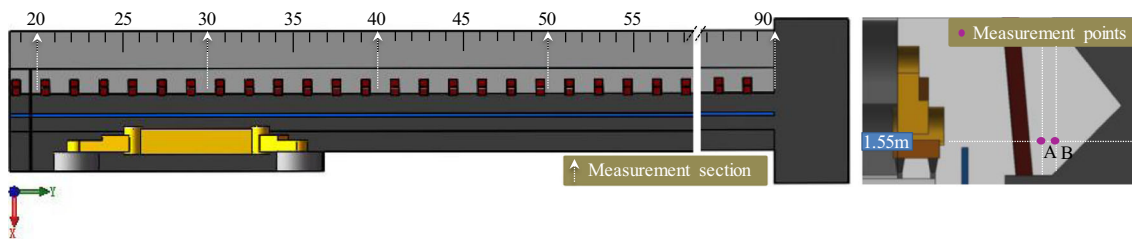
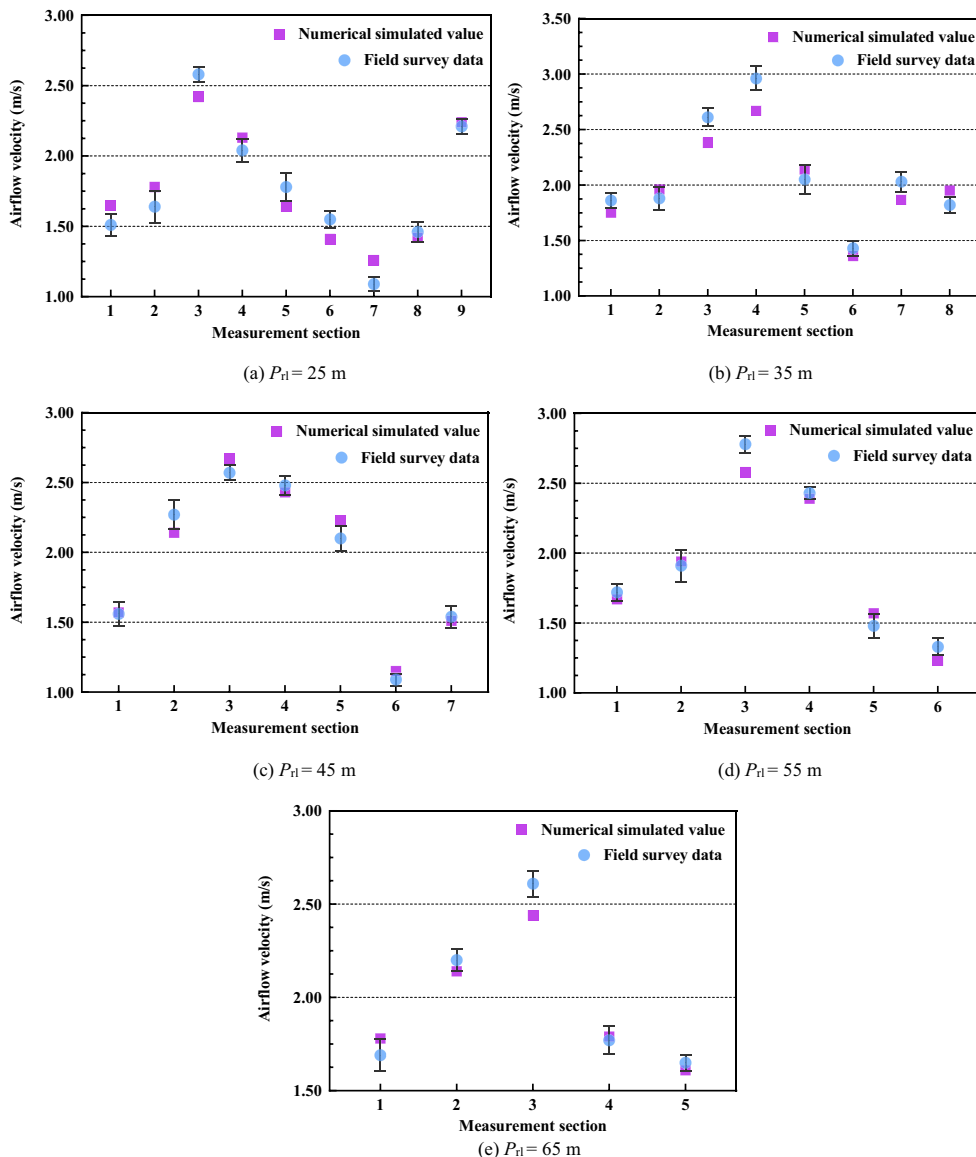


Fig. 5 Arrangement of airflow measurement sections and points for $P_{rl} = 35$ m

that the airflow at the end of the mining face can be fully developed; the surfaces of the static equipment, e.g., hydraulic supports, the cable trough, and the coal cutter, are all set as “no-slip wall.” Additionally, the following three assumptions are made in the present study: (1) hydraulic supports, cable trough, and coal cutter are all fixed; (2) temperature field remains unchanged; and (3) air in the fluid domain is incompressible.

Due to the large mining height, dust particles produced in support movement primarily accumulates at the top of the mining face, posing limited threat to workers, and only a small number of dust particles are carried to the air inlet (Nie et al. 2018; Petrov et al. 2014; Cong et al. 2014). Therefore, the present study only focuses on the dust production during the coal cutting process, which generates significant amount of dust. According to the air quality index PM 2.5 and the critical

Fig. 6 Comparison between measured and simulated airflow velocity, where a $P_{rl} = 25$ m, b $P_{rl} = 35$ m, c $P_{rl} = 45$ m, d $P_{rl} = 55$ m, e $P_{rl} = 65$ m



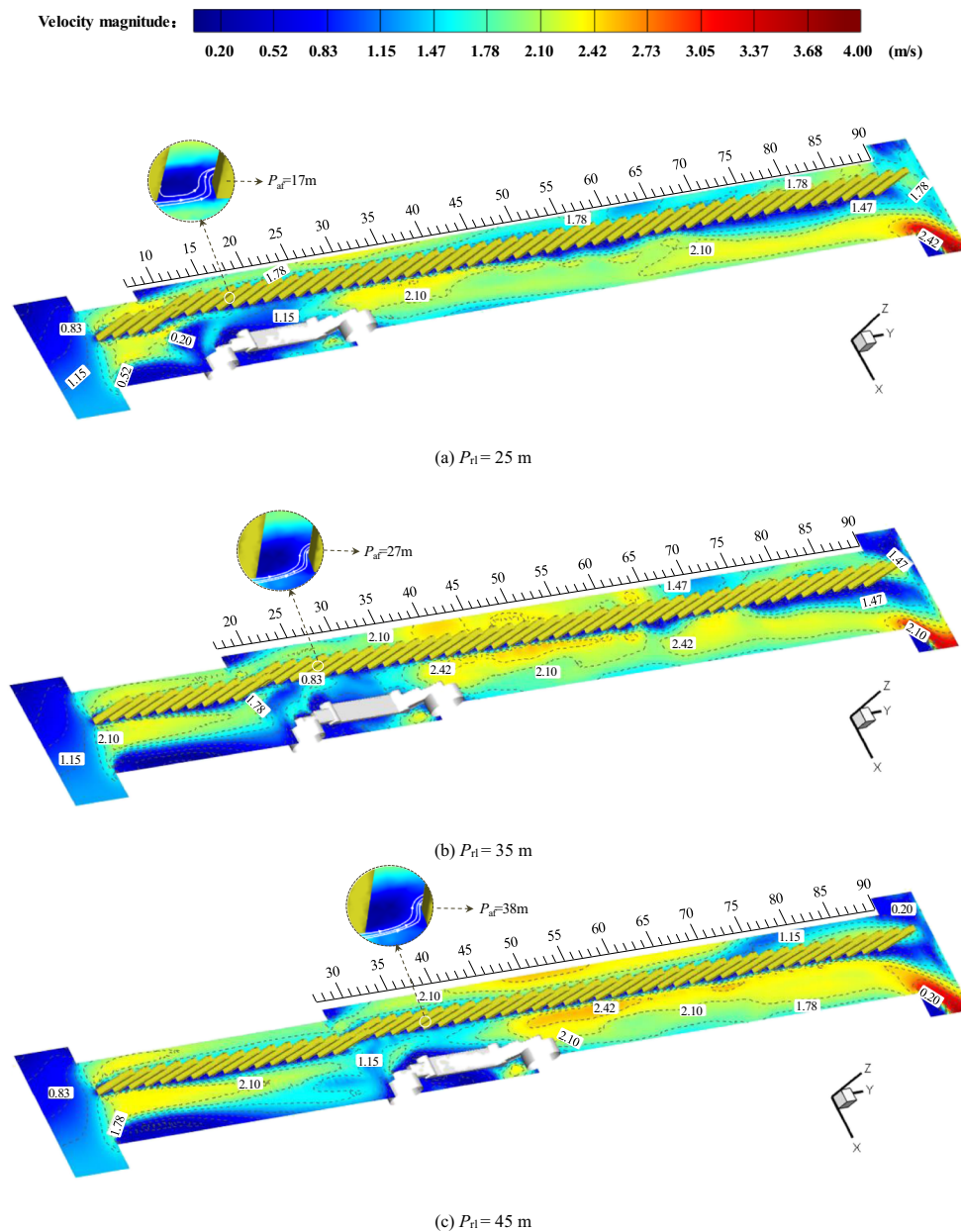


Fig. 7 Migration behaviors of airflow field for different coal cutter locations, where **a** $P_{H1} = 25$ m, **b** $P_{H1} = 35$ m, **c** $P_{H1} = 45$ m, **d** $P_{H1} = 55$ m, **e** $P_{H1} = 65$ m

diameter of the respirable dust particles, the present study lays emphasis on the distribution of dust particles with the sizes being 2.5, 7, 20, 40, and 80 μm , respectively, so as to quantitatively characterize the behavior of dust particles with different sizes. Table 1 lists the detailed settings of dust parameters, mainly including total flow rate, drag law, and particle type (Zhang et al. 2018; Ding et al. 2017; Zhou et al. 2017; Sasmito et al. 2013).

Field validation

For validating the accuracy of the present numerical simulation results, the present study measures airflow velocities at the height of the respiratory zone along the footway in the no. 5301 mining face of Tangkou Mine with coal cutter operated

at different locations. In the present study, the height of the respiratory zone is set to 1.55 m, where most workers breathe. In accordance with the size of this face and the practical conditions, multiple airflow measurement sections are set up on the leeward side of the rear drum at an interval of 10 m. Figure 5 shows the arrangement of airflow measurement points for $P_{H1} = 35$ m. Airflow velocities at points A and B are measured by an anemometer (TSI8455) for several times to obtain average values. Figure 6 compares the measured airflow velocities (L) with the simulation results at 1.55 m along the footway with the coal cutter operated at different locations. The relative error, denoted as δ , can be calculated as $\delta = \frac{\Delta}{L} \times 100\%$, where Δ denotes the difference between the simulated value and the measured value.

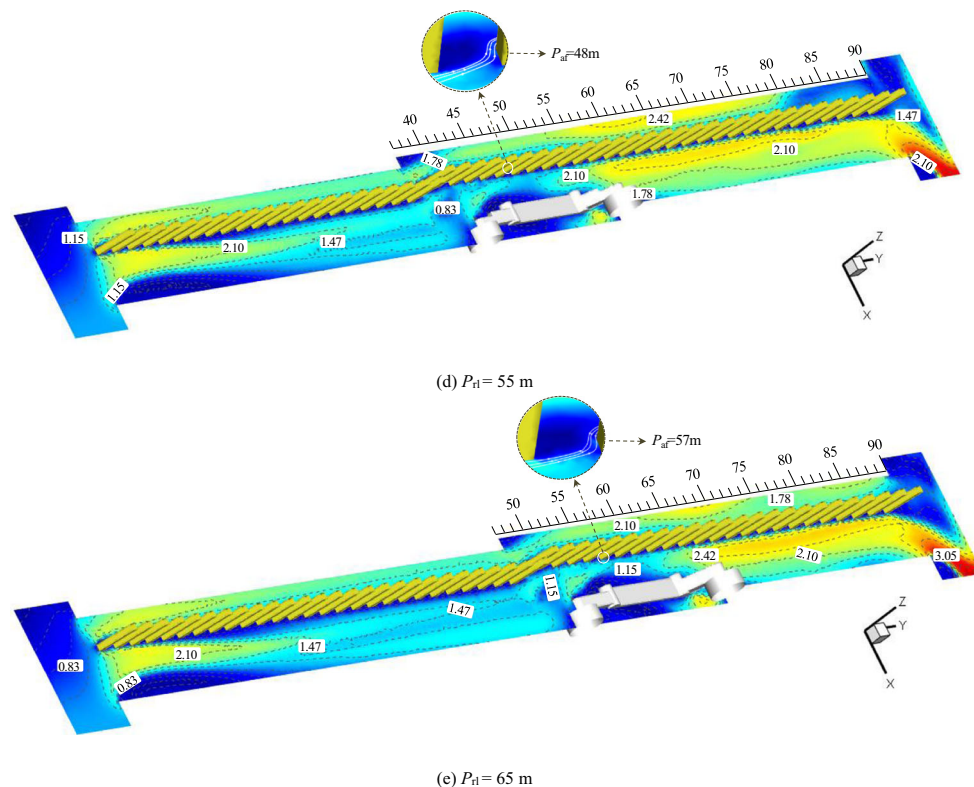


Fig. 7 (continued)

Through comparison, it can be observed that both measurement and simulation results exhibit almost identical variation tendencies at the height of respirable zone on the footway along the positive direction of y -axis, suggesting that the overall accuracy of the simulated airflow migration patterns at the fully mechanized mining face is decent. A deviation of 0.63~13.49% between the measured and the simulated airflow velocities can be observed; however, considering the complexity of the operating environment and many uncontrollable factors in airflow measurement process, this error range is acceptable. Accordingly, it can be concluded that the present numerical simulation of airflow field is satisfactorily representative of the reality.

Analysis of numerical simulation results

Analysis of numerical simulation results of airflow field

Significant dust dispersion and pollution can be observed in a large-mining-height fully mechanized mining face. Since the dust produced by coal cutting is dispersed to the operating region by airflow, one should first analyze the migration patterns of airflow before investigating the dynamic dispersion behaviors of dust particles in the fully mechanized mining face. The migration behaviors of airflow field at different coal-cutting locations of the mining face are then simulated using ANSYS.

As shown in Fig. 7, airflow velocity first decreases and then increases along the positive direction of y -axis. Airflow enters the fully mechanized mining face via the inlet airway and then moves towards the footway due to the existence of coal cutter. Airflow velocity drops to below 1.15 m/s around the coal cutter, and then increases steadily at the front drum and is eventually stabilized between 1.78 and 2.42 m/s. At the end of the mining face, the airflow direction exhibits a rapid change, and the velocity also increases from 2.10 to 4 m/s.

Additionally, due to the disturbing influence of coal cutter, airflow deviates towards the negative direction of x -axis, and a small amount of airflow is squeezed into the footway region. For $P_{r1} = 25, 35, 45, 55,$ and 65 m, the locations where airflow enters the footway on the leeward side of the support movement (denoted as P_{af}) are 17, 27, 38, 48, and 57 m, respectively. Through polynomial curve fitting, the correlation between P_{r1} and P_{af} can be written as: $P_{af}(P_{r1}) = -0.0021P_{r1}^2 + 1.2029P_{r1} - 11.961$ ($R^2 = 0.9996$).

Analysis of airflow-dust coupled migration results

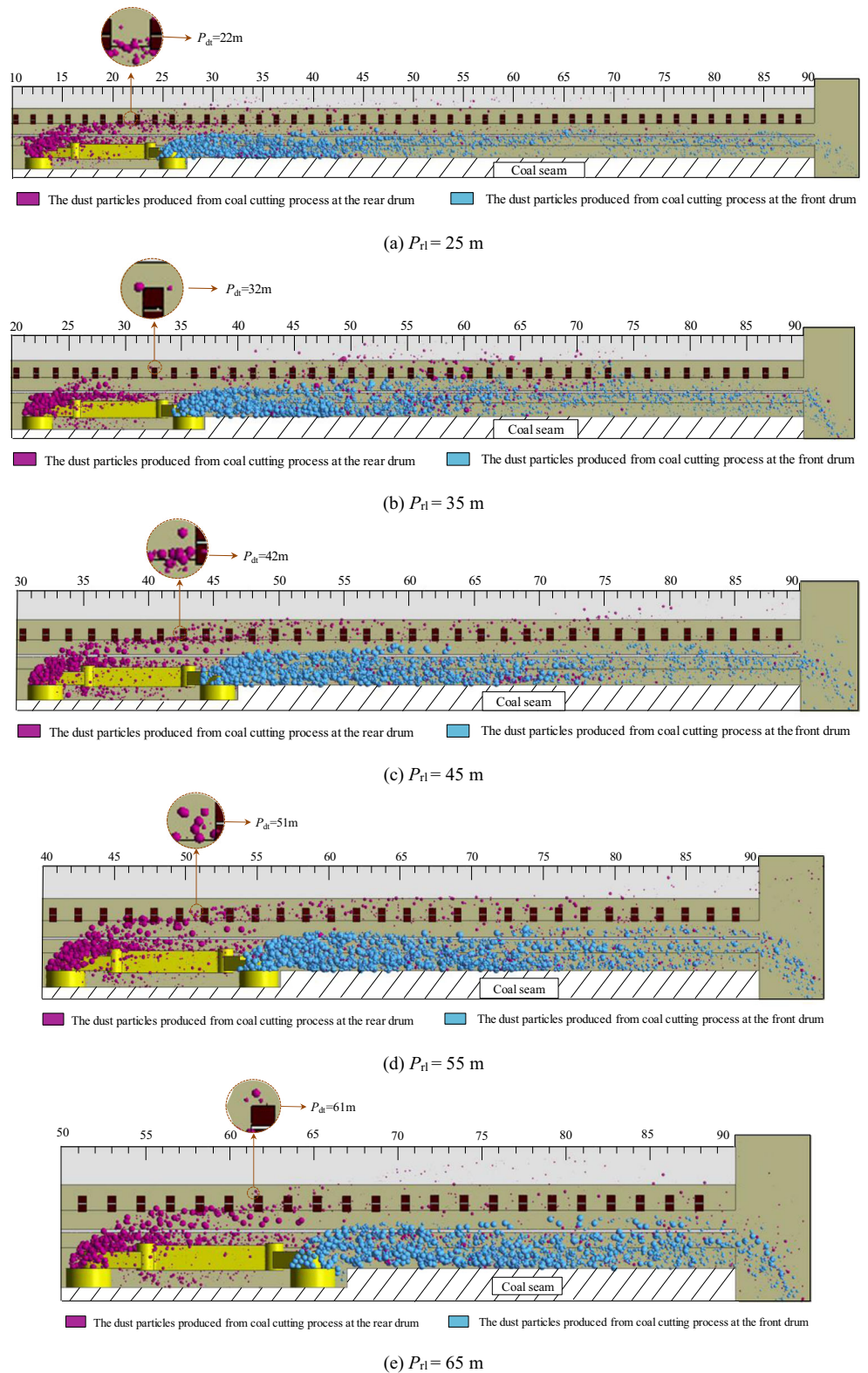
Dust dispersion patterns with coal cut at different locations

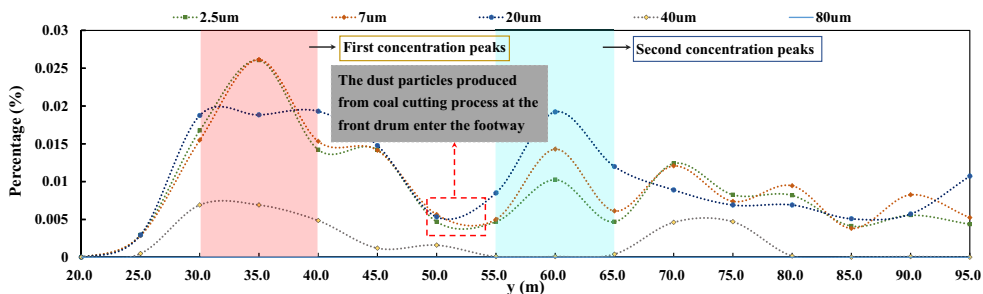
In a large-mining-height fully mechanized mining face, a great amount of dust is produced during coal cutting process, which is in turn dispersed to the entire mining face

within a short period of time. To facilitate the observation of the dust dynamic dispersion patterns with the coal cutter operated at different locations, the airflow-dust coupled migration processes under these different conditions are

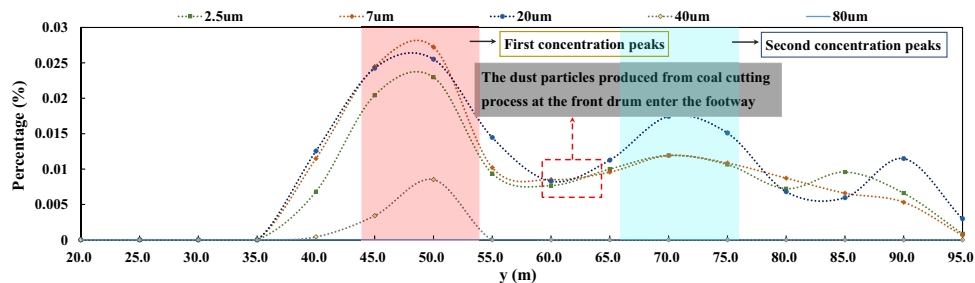
simulated and analyzed, with the results shown in Fig. 8. In order to distinguish the dispersion patterns associated with the dust with different sizes in the fully mechanized mining face, dust particles are magnified by the same

Fig. 8 Distribution of dust particles in the fully mechanized mining face for different coal cutter locations, where **a** $P_{r1} = 25$ m, **b** $P_{r1} = 35$ m, **c** $P_{r1} = 45$ m, **d** $P_{r1} = 55$ m, **e** $P_{r1} = 65$ m

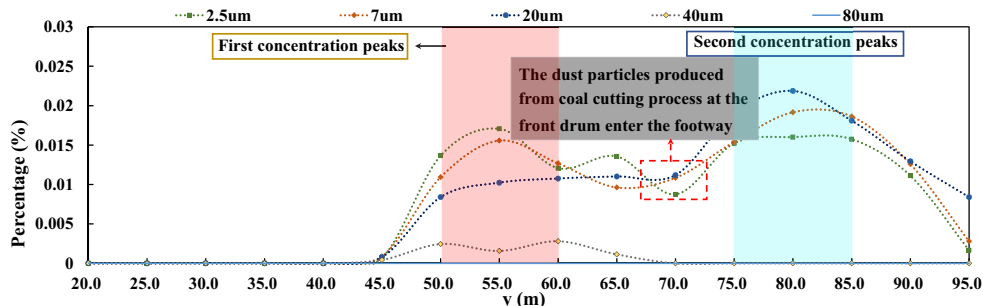




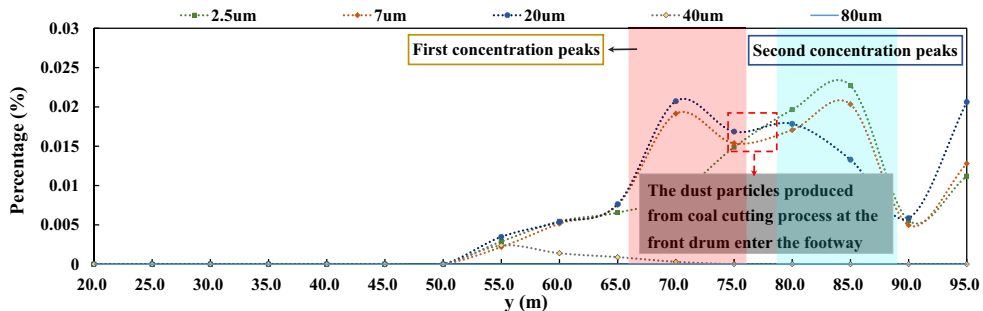
(a) $P_{fl} = 25$ m



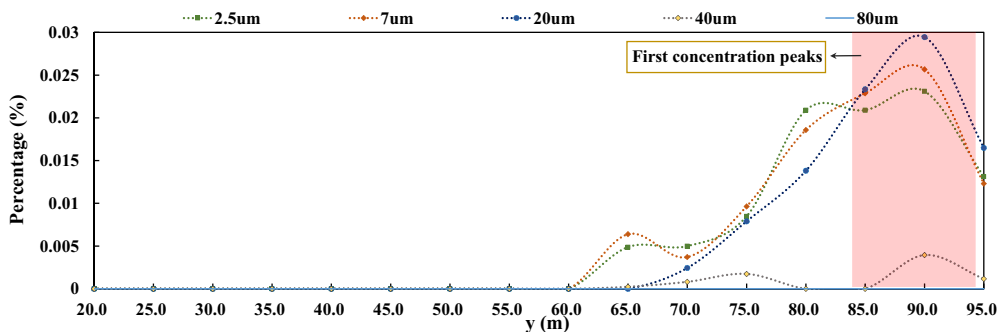
(b) $P_{fl} = 35$ m



(c) $P_{fl} = 45$ m



(d) $P_{fl} = 55$ m



(e) $P_{fl} = 65$ m

◀ **Fig. 9** Variations of the produced dust particles with different sizes in the respiratory zone on the footway for different coal cutter locations, where a $P_{ri} = 25$ m, b $P_{ri} = 35$ m, c $P_{ri} = 45$ m, d $P_{ri} = 55$ m, e $P_{ri} = 65$ m

scaling factor; moreover, dust particles are marked with two colors to better differentiate the dust particles produced from the front and rear drums.

The following conclusions can be drawn from Fig. 8.

- (1) The dust particles produced from coal cutting at the rear drum exhibit two different dispersion behaviors after a 5-m migration. A small fraction of dust is disturbed by airflow and then enters the footway, while a large fraction of dust continues to move towards the end of the tunnel. The dust produced from coal cutting at the front drum is slightly affected by the airflow and is thereby mostly carried by airflow from the mining face. The dust particles produced from coal cutting by two drums are all dispersed slowly to the footway on the leeward side.
- (2) As the dust is settled during the migration process in the fully mechanized mining face, the number of large dust particles is gradually reduced while small dust particles are stably suspended in the air. Accordingly, dust particles with different sizes differ greatly in terms of the dispersion range in the fully mechanized mining face, and the dust particles posing threat to workers exhibit different distribution patterns in different regions.
- (3) The dust particles produced from coal cutting at different locations enter the footway at different locations. For $P_{ri} = 25, 35, 45, 55,$ and 65 m, the locations where dust particles enter the footway (denoted as P_{dt}) are 22, 32, 42, 51, and 61 m, respectively. The correlation between P_{ri} and P_{dt} can be fitted as: $P_{dt}(P_{ri}) = -0.0007P_{ri}^2 + 1.0343P_{ri} - 3.3536$ ($R^2 = 0.9998$). Through comparison, the correlation between P_{dt} and P_{af} can be written as: $P_{dt}(P_{ri}) = P_{af}(P_{ri}) + \delta_{dfc}$ ($3 \leq \delta_{dfc} \leq 5$).

Distribution patterns of dust particles with different sizes at the respiratory height on the footway

Workers generally stay for an extended period of time on the footway in the fully mechanized mining face, and the dust particles dispersed to the respiratory zone are main sources causing pneumoconiosis (Hu et al. 2017; Liu et al. 2007; Niu et al. 2010; Zhang et al. 2014). The present study examines the statistical dust concentration pattern in the respiratory zone on the footway (i.e., $x = -6.0 \sim -5.2$ m and $y = 1.45 \sim 1.55 + 0.5$ m). Using MATLAB code, the percentages the dust particles with five different sizes in the respiratory zone on the footway account for in the total dust particles produced in

the mining face are calculated, with the statistical results shown in Fig. 9.

It can be observed from Fig. 9 that:

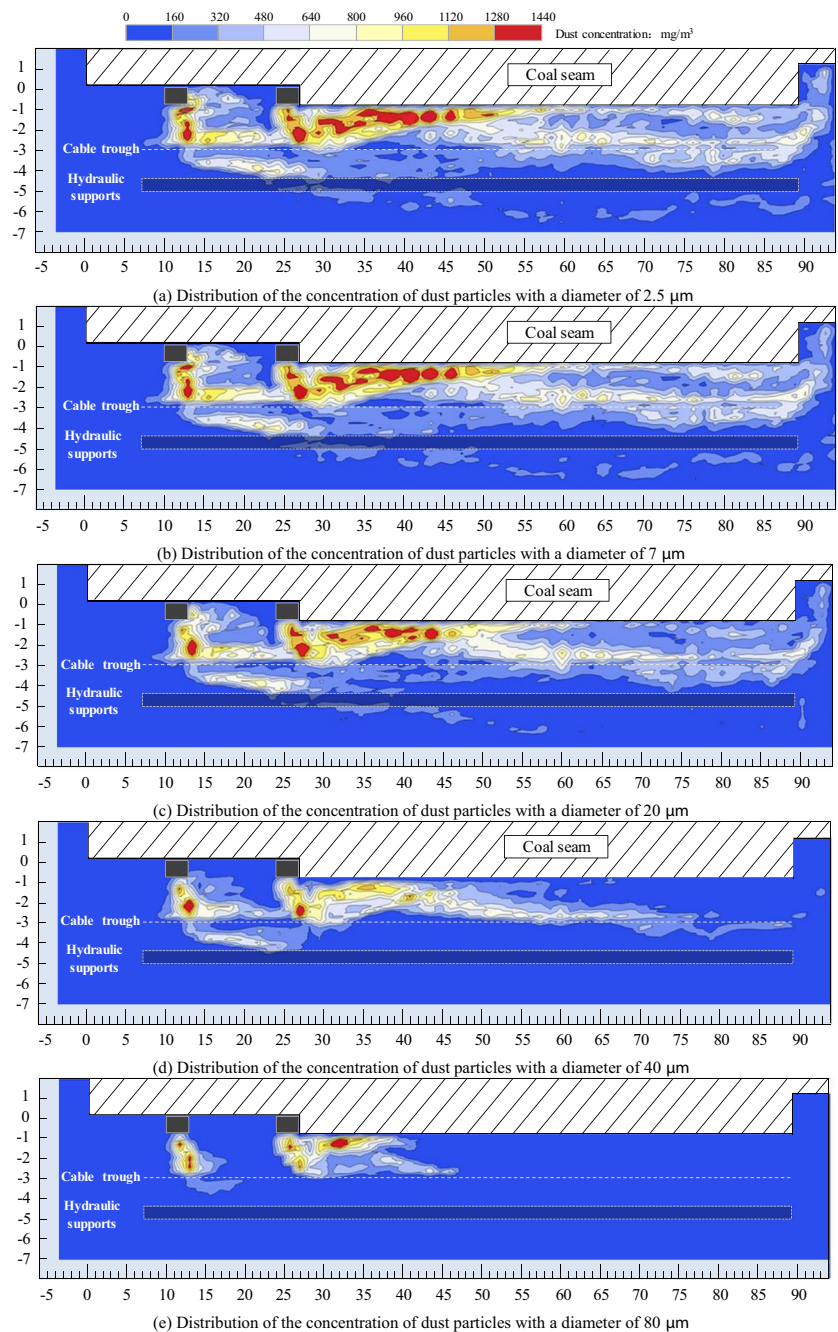
- (1) The dust particles produced from coal cutting process at the rear drum enter the footway before those produced at the front drum, which can account for the first and second peaks of the dust concentrations in the respiratory zone on the footway. For $P_{ri} = 25, 35, 45, 55,$ and 65 m, first concentration peaks associated with different dust sizes appear at $y = 30 \sim 40$ m, $44 \sim 54$ m, $50 \sim 60$ m, $66 \sim 76$ m, and $84 \sim 94$ m, respectively, followed by the second peaks at $y = 55 \sim 65$ m, $66 \sim 76$ m, $75 \sim 85$ m, and $79 \sim 89$ m, respectively (it should be noted that when $P_{ri} = 65$ m, no second concentration peaks can be observed due to the exceptional short dispersion process). Dust suppression measures are mainly implemented in the regions around the aforementioned first and second peaks.
- (2) With an increase of P_{ri} , the percentages of dust particles 2.5, 7, and 20 μm in diameter in the respiratory zone on the footway drop from 0.14, 0.15, and 0.16% to 0.09, 0.09, and 0.09%, respectively. The dust particles 40 μm in diameter are mainly settled due to strong gravity, and only a large number of dust particles accumulated in a few regions near the coal cutting location, whose maximum percentage in the dust produced in the mining face is only 0.03%. The dust particles with a diameter of 80 μm do not enter the respiratory zone on the footway during the entire coal cutting process.

Concentration distribution and settling patterns of the dust particles with different sizes at a large-mining-height fully mechanized mining face

During coal cutting process in a large-mining-height fully mechanized mining face, the dust particles with different sizes are affected by airflow and gravity to different degrees. The present study divides the x - y plane of the fully mechanized mining face into a mesh of $0.5 \text{ m} \times 0.5 \text{ m}$ grid blocks for analyzing the statistical dispersion patterns of the dust particles with different sizes in this large-mining-height fully mechanized mining face. For $P_{ri} = 25$ m, dust particles are dispersed further away, and we will focus on this condition for further analysis, with the corresponding simulation results shown in Fig. 10.

As shown in Fig. 10, the dust particles with different sizes exhibit significantly different concentration distributions and settling regions in the large-mining-height fully mechanized mining face. The dust particles with the diameters of 2.5, 7, and 20 μm show similar dispersion ranges in the mining face. Due to the superposition of the dust

Fig. 10 Distributions of dust particle concentration with different sizes, where **a** distribution of the concentration of dust particles with a diameter of $2.5\ \mu\text{m}$, **b** distribution of the concentration of dust particles with a diameter of $7\ \mu\text{m}$, **c** distribution of the concentration of dust particles with a diameter of $20\ \mu\text{m}$, **d** distribution of the concentration of dust particles with a diameter of $40\ \mu\text{m}$, **e** distribution of the concentration of dust particles with a diameter of $80\ \mu\text{m}$



particles produced in coal cutting by front and rear drums, dust concentration 25 m on the leeward side of the coal cutter reaches a maximum of $1440\ \text{mg}/\text{m}^3$, and dust concentration in return airway is up to $960\ \text{mg}/\text{m}^3$; due to the disturbing effect of the rear drum, dust enters the footway along the negative direction of x -axis, where the concentration can reach up to $800\ \text{mg}/\text{m}^3$. Under the gravity, the dust particles with a size of $40\ \mu\text{m}$ are significantly settled, and dust concentration keeps dropping in the dispersion process with airflow until it reaches zero. The dust particles with a diameter of $80\ \mu\text{m}$ are significantly affected by gravity and

are only retained in front of the supports, while most of dust particles are dispersed to the drums within a range of 22 m on the leeward side of the coal cutter.

Conclusions

Based on gas/solid two-phase flow method, the present study establishes an airflow-dust coupled model in a large-mining-height fully mechanized mining face and analyzes migration characteristics of airflow and microscale dispersion patterns of

the dust particles with different sizes with the coal cutter operated at different locations through simulation. By comparison, the mean relative error between measured airflow velocities and the simulation results is smaller than 14%, which can validate the accuracy of the present simulation results of airflow field.

- (1) In the large-mining-height fully mechanized mining face, airflow velocity along the positive direction of y -axis first decreases and then increases. Airflow deviates towards the negative direction of x -axis and enters the footway. Driven by airflow, the dust particles produced during coal cutting at different locations enter the footway at different locations. By means of polynomial curve fitting, the correlation between P_{dt} and P_{rl} can be written as: $P_{dt}(P_{rl}) = -0.0007P_{rl}^2 + 1.0343P_{rl} - 3.3536$ ($R^2 = 0.9998$), while the correlation between P_{dt} and P_{af} can be written as: $P_{dt}(P_{rl}) = P_{af}(P_{rl}) + \delta_{dfc}$ ($3 \leq \delta_{dfc} \leq 5$).
- (2) The dust particles produced during coal cutting by the rear drum enters the footway earlier than those produced by the front drum. Accordingly, first and second-peaks of dust concentration at the respiratory zone on the footway appear. With the increase of P_{rl} , the fractions of the dust particles with the diameters of 2.5, 7, and 20 μm at the respiratory zone on the footway in the total dust drop from 0.14, 0.15, and 0.16% to 0.09, 0.09, and 0.09%, respectively. More dust particles with a diameter of 40 μm accumulate in a few regions near the coal cutting location, which maximum percentage only 0.03% of total dust produced in the mining face. The dust particles with a diameter of 80 μm do not enter the respiratory zone on the footway during the entire coal cutting process.
- (3) The dust particles with different sizes differ greatly in concentration distribution and settling region. Due to the superposition of concentration fields of dust particles with the sizes of 2.5, 7, and 20 μm , dust concentration 25 m on the leeward side of the coal cutter can reach up to 1440 mg/m^3 . Driven by airflow, the concentration of dust particles with a diameter of 40 μm drops steadily and approaches 0 at the return corner. The dust particles with a diameter of 80 μm are mostly distributed around the drums within the range of 22 m on the leeward side of the coal cutter.

References

- Cheng W, Nie W, Qi Y, Yao Y (2012) Research on diffusion rule of dust pollution in coal mine whole-rock fully mechanized workplace. *J Converg Inf Technol* 7:728–736
- Cheng W, Yu H, Zhou G, Nie W (2016) The diffusion and pollution mechanisms of airborne dusts in fully-mechanized excavation face at mesoscopic scale based on CFD-DEM. *Process Saf Environ Prot* 104:240–253
- Cheng WM, Hu XM, Xie J, Zhao YY (2017) An intelligent gel designed to control the spontaneous combustion of coal: fire prevention and extinguishing properties. *Fuel* 210:826–835
- Cong T, Jiang ZA, Chen JS, Pei W (2014) Numerical simulation of influencing factors on dust movement during coal cutting at fully mechanized working faces. *J Univ Sci Technol Beijing* 36:716–721
- Courtney WG, Cheng L, Divers EF (1986) Deposition of respirable coal dust in an airway. Report of investigations/1986. *Chinese J Pathophysiol* 17:1175–1178
- Ding C, He XQ, Nie BS (2017) Numerical simulation of airflow distribution in mine tunnels. *Int J Min Sci Technol* 27(4):663–667
- Fan T, Zhou G, Wang J (2018) Preparation and characterization of a wetting-agglomeration-based hybrid coal dust suppressant. *Process Saf Environ Prot* 113:282–291
- Hodkinson JR (1960) The relation between ventilation airspeed and respirable airborne-dust concentration in coalmines. *Colliery Eng*
- Hu ZX, Hu XM, Cheng WM, Lu W (2017) Influence of synthetic conditions on the performance of melamine-phenol-formaldehyde resin microcapsules. *High Perform Polym* 095400831875848
- Jia M, Fu Y, Yuan Y, Wei H, Sun S, Li J (2016) Migration law of respirable dust on a super-long fully mechanized double-shearer working face. *Int J Min Sci Technol* 26:1109–1115
- Klemens R, Kosinski P, Wolanski P, Korobeinikov VP, Markov VV, Menshov IS, Semenov IV (2001) Numerical study of dust lifting in a channel with vertical obstacles. *J Loss Prev Process Ind* 14:469–473
- Kurnia J, Candra et al (2014) Dust dispersion and management in underground mining faces. *Int J Min Sci Technol* 24:39–44
- Liang YP, Li B, Yuan Y et al (2017) Moving type of key strata and its influence on ground pressure in fully mechanized mining face with large mining height. *J China Coal Soc* 42:1380–1391
- Liu Y, Jiang Z, Cai W et al (2007) Numerical simulation of the dust movement rule in fully-mechanized coal faces. *J Univ Sci Technol Beijing* 29:351–353+362
- Liu Z, Cheng K, Li H, et al (2017a) Exploring the potential relationship between indoor air quality and the concentration of airborne culturable fungi: a combined experimental and neural network modeling study. *Environ Sci Pollut Res* 1–8
- Liu Z, Li H, Cao G (2017b) Quick estimation model for the concentration of indoor airborne culturable bacteria: an application of machine learning. *Int J Environ Res Public Health* 14:857
- Liu Q, Nie W, Hua Y, Peng H, Liu Z (2018) The effects of the installation position of a multi-radial swirling air-curtain generator on dust diffusion and pollution rules in a fully-mechanized excavation face: a case study. *Powder Technol* 329:371–385
- Nie W, Liu Y, Wei W, Hu X, Ma X, Peng H (2016) Effect of suppressing dust by multi-direction whirling air curtain on fully mechanized mining face. *Int J Min Sci Technol* 26:629–635
- Nie W, Wei W, Liu Q et al (2018) Simulation experiments on the controllability of dust diffusion by means of multi-radial vortex airflow. *Adv Powder Technol* 29:835–847
- Niu W, Jiang Z, Liu Y (2010) Numerical simulation on dust movement regularities at fully-mechanized coal faces and its utilization. *J Liaoning Tech Univ* 29:357–360
- Patankar NA, Joseph DD (2001) Modeling and numerical simulation of particulate flows by the Eulerian–Lagrangian approach. *Int J Multiph Flow* 27:1659–1684
- Petrov T, Wala AM, Huang G (2014) Parametric study of airflow separation phenomenon at face area during deep cut continuous mining. *Min Technol* 122:208–214

- Ren T, Wang Z, Cooper G (2014) CFD modelling of ventilation and dust flow behaviour above an underground bin and the design of an innovative dust mitigation system. *Tunn Undergr Sp Technol* 41: 241–254
- Sa Z, Li F, Qin B, Pan X (2012) Numerical simulation study of dust concentration distribution regularity in cavern stope. *Saf Sci* 50: 857–860
- Sasmito AP, Birgersson E, Ly HC, Mujumdar AS (2013) Some approaches to improve ventilation system in underground coal mines environment—a computational fluid dynamic study. *Tunn Undergr Sp Technol* 34:82–95
- Shi XX, Jiang ZA, Zhou SY, Cai W (2008) Experimental study on dust distribution regularity of fully mechanized mining face. *J China Coal Soc* 33:1117–1121
- Toraño J, Tomo S, Menéndez M, Gent M (2011) Auxiliary ventilation in mining roadways driven with roadheaders: validated CFD modelling of dust behaviour. *Tunn Undergr Sp Technol* 26:201–210
- Wang P, Feng T, Liu R (2011) Numerical simulation of dust distribution at a fully mechanized face under the isolation effect of an air curtain. *Int J Min Sci Technol* 21:65–69
- Wang J, Yang S, Kong D (2016) Failure mechanism and control technology of longwall coalface in large-cutting-height mining method. *Int J Min Sci Technol* 26:111–118
- Wang H, Cheng W, Sun B, Ma Y (2017a) Effects of radial air flow quantity and location of an air curtain generator on dust pollution control at fully mechanized working face. *Adv Powder Technol* 28: 1780–1791
- Wang H, Nie W, Cheng W et al (2017b) Effects of air volume ratio parameters on air curtain dust suppression in a rock tunnel's fully-mechanized working face. *Adv Powder Technol* 29:230–244
- Yu H, Cheng W, Wu L, Wang H, Xie Y (2017) Mechanisms of dust diffuse pollution under forced-exhaust ventilation in fully-mechanized excavation faces by CFD-DEM. *Powder Technol* 317: 31–47
- Zhang G, Shang S, Wu W (2014) Coal dust concentration distribution of fully-excavating working face by modeling analysis. *J Liaoning Tech Univ* 33:456–460
- Zhang Q, Zhou G, Qian X, Yuan M, Sun Y, Wang D (2018) Diffuse pollution characteristics of respirable dust in fully-mechanized mining face under various velocities based on CFD investigation. *J Clean Prod* 184:239–250
- Zhou G, Zhang Q, Bai R, Fan T, Wang G (2017) The diffusion behavior law of respirable dust at fully mechanized caving face in coal mine: CFD numerical simulation and engineering application. *Process Saf Environ Prot* 106:117–128
- Zhou G, Ma Y, Fan T, Wang G (2018) Preparation and characteristics of a multifunctional dust suppressant with agglomeration and wettability performance used in coal mine. *Chem Eng Res Des* 132:729–742